

Microstructure and Mechanical Properties of $\text{Ti}_{50}\text{Ni}_{(50-x)}\text{Fe}_x$ Alloys Fabricated by Powder Metallurgy Process



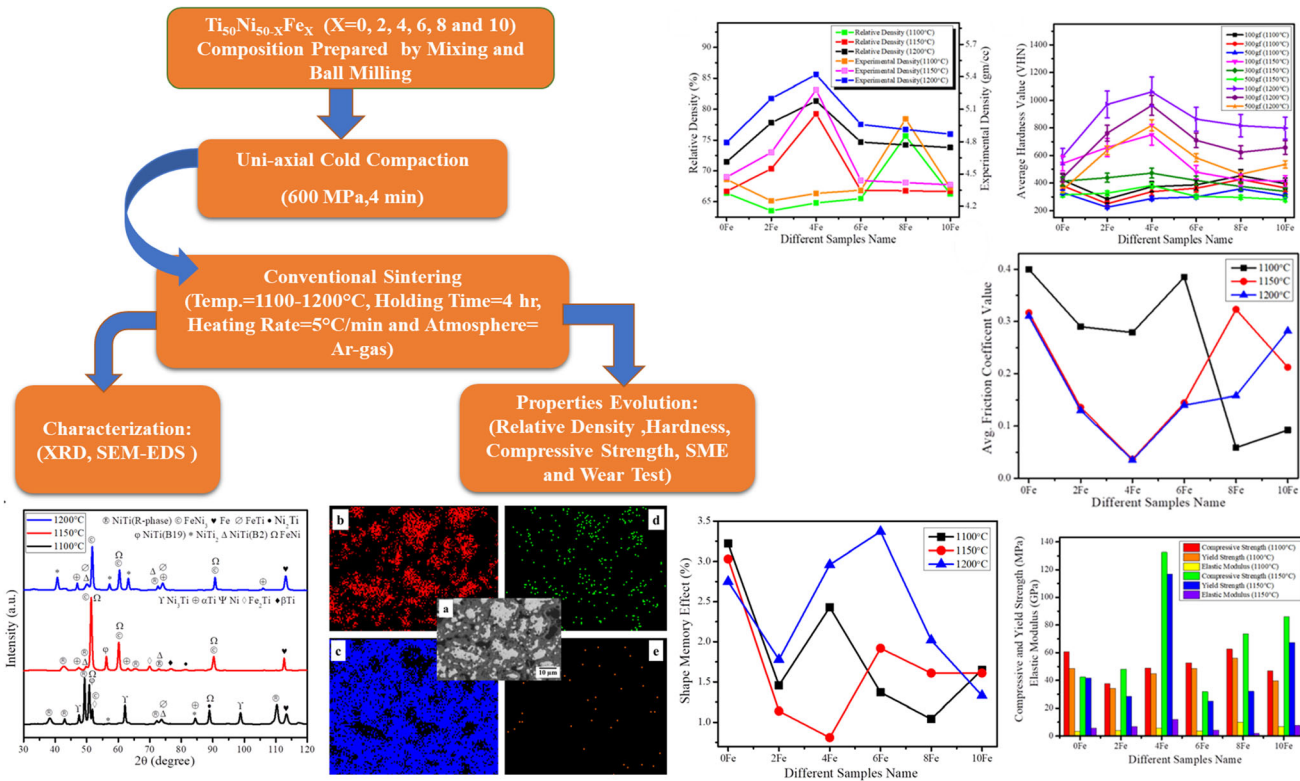
JAGADISH PARIDA, SUBASH CHANDRA MISHRA, and AJIT BEHERA

This paper investigates the microstructure and mechanical properties of $\text{Ti}_{50}\text{Ni}_{(50-x)}\text{Fe}_x$ alloys fabricated by powder metallurgy technique. Here, sintering temperatures varied from 1100 °C to 1200 °C for the compacted milled powder mixture. Microstructure, chemical composition, phase formation, porosity, density, hardness, wear, shape memory effect, and compressive strength of the sintered sample were carried out using SEM, EDS, XRD, and mechanical tests, respectively. The SEM and XRD analysis results show that the microstructure of alloys consists of (Ni, Fe)-rich, Ti-rich phases with less retained pore. The densification and hardness increase with increasing the sintering temperature. The 4 at. pct Fe sample sintered at 1200 °C shows higher densification, a lower friction coefficient, and a higher hardness value. The 4 at. pct Fe sample sintered at 1150 °C shows higher compressive, and yield strengths of 132.57 and 116.86 MPa, respectively, and the 6 at. pct Fe sample sintered at 1200 °C shows a higher shape memory effect of 3.37 pct, which are higher in comparison to other compositions and other sintering temperature samples. Abrasive wear of the sample has been carried out, and it found that there is a decrease in friction coefficient value with an increase in sintering temperature from 1150 °C to 1200 °C of the sample.

JAGADISH PARIDA, SUBASH CHANDRA MISHRA, and AJIT BEHERA are with the Department of Metallurgical and Materials Engineering, National Institute of Technology, Rourkela, Odisha, 769008, India. Contact e-mail: beheraajit@nitrkl.ac.in

Manuscript submitted November 12, 2022; accepted March 14, 2023.

Article published online April 12, 2023



<https://doi.org/10.1007/s11661-023-07037-5>

© The Minerals, Metals & Materials Society and ASM International 2023

I. INTRODUCTION

SHAPE memory characteristics and transformation behavior are affected by third alloying elements that are added to the binary NiTi shape memory alloys. In other words, various techniques are used to alter the properties of binary NiTi-alloys by adding different alloying elements. For example, Fe, Cu, and Al are responsible for the decrease in transformation temperature, whereas elements like Pt, Pd, Zr, Au, and Hf are responsible for the increase in transformation temperature.^[1-3] The third alloying element addition not only changes the transformation temperature but also changes the transformation path and the product stoichiometry. For example, NiTi shows a B2 → B19' transformation directly, but with the Fe addition as the third alloying element, the TiNiFe alloy shows a two-stage transformation, *i.e.*, B2 → R → B19'. Also, it is seen that when Fe content increases, transformation B2 → R is more separated from the R → B19' transformation.^[4] Therefore, the TiNiFe alloy is mostly useful for studying the intermediate phase (called the R-phase).^[5] Choi *et al.*^[6] found that an 8 pct iron addition to Ni_{50-x}Ti₅₀Fe_x will completely suppress phase transformations, and the parent phase does not transform. Compared to the binary NiTi alloy, the ternary TiNiFe alloy generally shows low-temperature hysteresis, higher toughness,

higher corrosion resistance,^[7] radiopacity, and lower martensitic phase transformation temperatures.^[8] Due to the above properties, it is used for couplings in jet fighters/aircraft,^[9,10] pipe couplings for engineering applications,^[11] and actuator applications.^[12]

Generally, NiTi-based binary and ternary (*e.g.*, TiNiFe, *etc.*) alloys are produced by melting and casting techniques. However, the casting technique is expensive, and the mechanical properties are affected by unavoidable surrounding gases such as O₂, N₂, and H₂. NiTi-based alloys are directly affected by environmental conditions during their production by this liquid metallurgy technique.^[13] To avoid these limitations, the powder metallurgy (PM) technique is preferable.^[14,15] Different PM methods, like hot isostatic pressing, spark plasma sintering, and metal injection moulding, are used in NiTi-alloys production.^[16,17] Among all these processes, pressure-less sintering is used for NiTi-alloys due to the simplicity of the process as well as its low production cost. Pressure-less sintering is a type of PM method where green compact is heated to a predetermined temperature at which reactions take place between particles with the help of heat. Pressure-less sintering was already used to study the formation of various intermetallic compounds for NiTi binary and ternary systems (such as NiTiCu and NiTiAl).^[18-22]

Mechanical alloying (MA) is an effective practice for homogenization in the PM technique.^[23] By mechanical alloying, the predetermined chemical composition of NiTi SMA can be altered easily during fabrication.^[24–27]

NiTi-based alloys show better wear resistance compared to other well-known structural wear resistance materials, such as 304 stainless steel, GCr15 steel, nitride 38CrMoAlA alloy steel, and Co-based alloy.^[28–34] Hence, NiTi-based alloys are proven to be used in high wear-resistant structural and functional applications. The wear behaviors and mechanisms of NiTi alloy are studied under different conditions. It indicates that the better wear resistance of the alloy is due to its two peculiar behaviors, *i.e.*, shape memory effect (SME) and pseudoelasticity (PE), in relation to the martensitic variant accommodation.^[35,36] Generally, the wear resistance of materials depends on their mechanical properties, such as surface Young's modulus, toughness, hardness, and work-hardening.^[37,38] Singh and Alpas *et al.*^[39] show that the Ti₅₀Ni₄₇Fe₃ alloy wear rate is only 2–5 pct of the bearing steel (SAE 52100) wear rate. NiTi alloy shows three stages of wear during a wear behavior study against Al₂O₃ counter balls at different sliding distances and loads. The first is zero-wear (it gives a very small friction coefficient), the second is transition wear (the friction coefficient rapidly increases and then remains constant), and the third is abrasive wear (the friction coefficient increases because of wear debris).^[40] SME and PE behavior of the NiTi-based alloy can be observed in the first and second cases.

In this paper, ternary Ti₅₀Ni_(50-X)Fe_X alloy has been prepared by the powder metallurgy method with the variation of Fe percentage and sintering temperature to investigate the microstructure and mechanical properties. The phase evolution, microstructure, shape memory effect, and physical and mechanical properties of the prepared alloy have been carried out using XRD, SEM, EDS, indentation technique, hardness test, wear, and compression test. The densification process by pressure-less sintering and the effect on the shape memory property of TiNiFe alloy are the novel findings of this investigation.

II. MATERIALS AND METHODS

A. Sample Preparation

Commercial pure Ti (particle size: 45 μm, purity: 99 pct), Ni (particle size: 74–100 μm, purity: 99.8 pct), and Fe (particle size: 6–10 μm, purity: 99.5 pct) powders are procured from Alfa Aesar for the study. The powders were mixed according to atomic percentage in Ti₅₀Ni_{50-X}Fe_X (where X: 0, 2, 4, 6, 8, and 10 as mentioned in Table I) in a Turbula shaker mixer for 12 h and then dry milled/mechanically alloyed (milling time: 8 h, BPR: 10:1 and milling speed: 300 rpm) using a high-energy planetary ball mill with stainless steel vial and balls. The mill design and milling parameters details are discussed in our previous works.^[41] The milled powder composition was cold compacted at 600 MPa pressure with 4 min of holding time in a uniaxial press

Table I. Composition Abbreviation

Composition	Abbreviated Notation
Ti ₅₀ Ni ₅₀	0Fe
Ti ₅₀ Ni ₄₈ Fe ₂	2Fe
Ti ₅₀ Ni ₄₆ Fe ₄	4Fe
Ti ₅₀ Ni ₄₄ Fe ₆	6Fe
Ti ₅₀ Ni ₄₂ Fe ₈	8Fe
Ti ₅₀ Ni ₄₀ Fe ₁₀	10Fe

compaction machine (Nano Tec Bangalore, India). The compacted pellets were sintered at 1100 °C, 1150 °C, and 1200 °C for 4 h in a tubular furnace (heating and cooling rate: 5 °C/min) under Ar-atmosphere and then cooled in a furnace as shown in Figure 1(a).^[18] All the sintered samples were polished in a sequence, such as a belt grinder, emery paper, and diamond-pest-assisted cloth polishing for different characterization processes. The sintering temperature has been chosen to start at 1100 °C as per the phase diagram for better diffusion and densification. The given sintering temperature is higher than the lowest temperature of 942 °C and the 1085 °C liquidus line in the binary Ni–Ti and Fe–Ti phase diagram.

B. Characterization and Properties of the Sintered Sample

Thermal analysis of all compositions of the milled powders (30 mg) was done using a high-temperature differential scanning calorimeter (model: STAPT 1600 °C, make: Linseis GmbH, Germany) with a 10 °C/min heating rate from room temperature to 1500 °C under an Ar gas atmosphere in an alumina crucible. Phase analysis has been carried out using XRD (Philips PAN analytical diffractometer using Co radiations ($k = 1.79 \text{ \AA}$)) with constant parameters (*i.e.*, scan rate: 5 °/min, step size: 0.02 and 2θ range 30–120°). Morphology and compositional analysis have been carried out using SEM–EDS (make: Jeol, model: JSM-6480LV). The density and porosity values are measured by the Archimedes principle with the help of a density meter (model: Contech-CB300). Here, three readings are taken, and the average values are reported. Hardness values are calculated by the Vickers micro-hardness tester (make: Leco, model: LM248AT) with three different loads of 100, 300, and 500 gf for 10 s dwell times.^[42,43] For all samples, ten indentations are taken at each load and then calculated as average to get hardness values. The compression test (Instron digital UTM SATEC KN600) was carried out at room temperature with a strain rate of 0.1 mm/min and used to determine compressive strength, young modulus, and yield strength.^[44] The sample has a cylindrical shape with a H/D ratio of more than 0.8, based on ASTM standards. The wear behaviour (*i.e.*, wear depth and friction coefficient) is calculated by a ball-on-plate wear tester (make: Ducom, model: TR 208 M1) at room temperature in dry conditions using a spherical-shaped

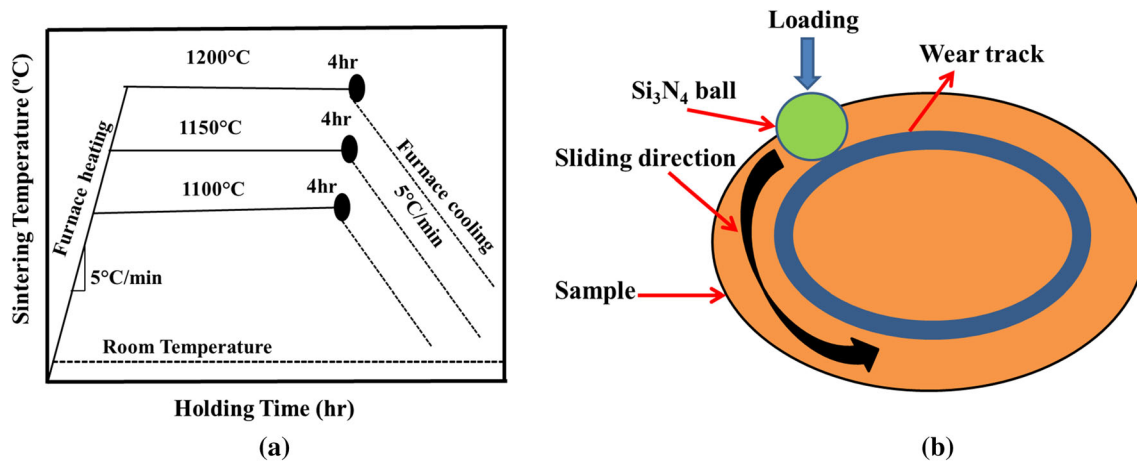


Fig. 1—Schematic diagrams of (a) the sintering process with the variation of temperature, and (b) ball-on-plate wear tester set-up.

ceramic Si₃N₄ ball (diameter: 2 mm) at a normal load, sliding speed, and time of 10 N, 30 rpm and 10 min, respectively.^[45] Figure 1(b) represents the schematic diagram of the ball-on-plate wear experimental set-up. The Vickers hardness tester is used to calculate the shape memory effect using the impression on the surface before and after providing thermal stimuli. Here the shape is deformed with the help of 1000 gf applied load for 10 s to calculate the average diameter (L_1). A deformed shape is followed by thermal energy stimulation that is heated up to 100 °C with 30 min of holding time in a vacuum furnace and then cooled in a furnace to calculate the average (L_2).^[46]

The shape memory effect was calculated using Eq. [1]^[46]:

$$\text{SME} = \frac{L_1 - L_2}{L_1} * 100 \quad [1]$$

III. RESULTS AND DISCUSSION

A. Thermal Analysis of Milled Powder

High-temperature differential scanning calorimetry (HTDSC) of the milled homogenized powder helps to find out the sintering temperature range and reaction behavior of the green compact. Figure 2 shows HTDSC for different homogenized TiNiFe powders heated from room temperature to 1500 °C with 10 °C/min. During heating, four exothermic peaks for milled powders 4Fe to 10Fe and three exothermic peaks for milled powders 0Fe and 2Fe are seen in the DSC graph. The four peaks have been seen in the temperature ranges of 186–343 °C, 410–528 °C, 1231–1296 °C and 1432–1458 °C, respectively. The first three exothermic peaks are not sharp (*i.e.*, very moderate), but the fourth peak is much sharper. Based on the Ni–Ti, Fe–Ni, and Fe–Ti phase diagrams, the first peak does not tally with any phase change, whereas the higher temperature peak indicates the corresponding phase change.^[47] Below the 400 °C sintering temperature, no reaction has taken place

between the powders. The second peak shows the inter-diffusion among Fe, Ti, and Ni to form the intermetallic compounds such as Ti₂Ni, FeTi, Fe₂Ti, and FeNi₃ phases. The fourth peak represents the melting point of the homogenized powder and also represents the higher exothermicity of the sample without iron (0Fe) than samples containing iron (2Fe, 4Fe, 6Fe, 8Fe, and 10Fe). So, it indicates a reaction that is processed by the presence of nickel in the milled powder. The enthalpy or heat release (ΔH) in exothermic reactions for different peaks in the temperature range 186 °C to 343 °C is – 42.12, – 75.07, – 74.73, – 62.26, – 80.82 and – 43.91 J/g and for 410 °C to 528 °C is – 70.04, – 48.06, – 101.6, – 14.71, – 89.17 and – 72.06 J/g for 0Fe, 2Fe, 4Fe, 6Fe, 8Fe, and 10Fe milled powder, respectively. Similarly, for 1231–1296 °C J/g is – 7.37, – 2.52, – 3.74, – 6.8 J/g for 4Fe, 6Fe, 8Fe, and 10Fe milled powder, and 1432 °C to 1458 °C is – 92.3, – 56.31, – 60.25, – 60.6, – 63.33, and – 54.67 J/g for 0Fe, 2Fe, 4Fe, 6Fe, 8Fe and 10Fe milled powder, respectively. The height of the peak (*i.e.*, the 4th peak) decreases with an increase in the Fe content from 0 to 4Fe. Further increase in Fe content up to 10 Fe leads to the formation of a new intermediate peak, *i.e.*, the 3rd peak in Figure 2. By comparing the exothermic reaction behavior of TiNiFe, it is observed from the 4th peak that less heat was released with increasing the percentage of Fe in the alloy. Less enthalpy of reaction at higher Fe content confirms the less energy dissipation in the NiTiFe composition.

B. Phase Analysis of Sintered Sample

Figures 3(a) through (f) shows the XRD analysis of all samples sintered at different temperatures. It is observed that NiTi (B2), NiTi (B19), NiTi (R), NiTi (B19'), NiTi₂, Ni₂Ti, Ni₃Ti, Ni₄Ti₃, FeTi, Fe₂Ti, and FeNi₃ phases are formed along with minor elemental forms (Ni, α -Ti, β -Ti, Fe). At 1100 °C sintering temperature, the major and secondary phase peaks of Ni, Fe, α -Ti, and β -Ti can be observed with some minor peaks such as NiTi, FeTi, Ni₃Ti, and Ni₂Ti, *etc.*, which is

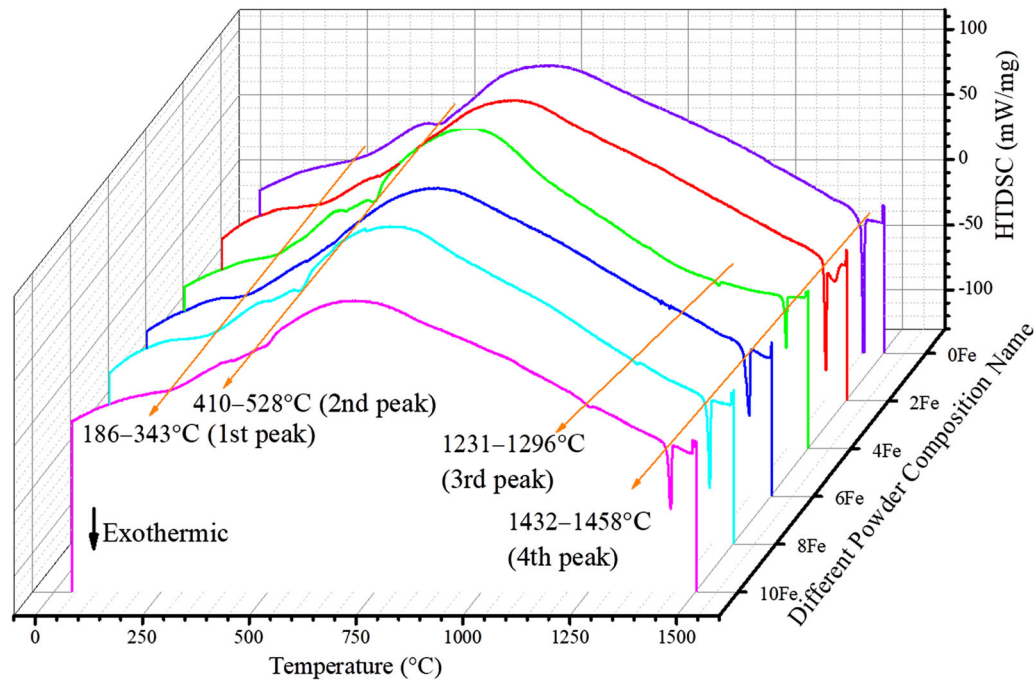


Fig. 2—DSC curves for different compositions of milled powder.

because of the insufficient sintering. As the temperature increases, the diffusion rate of Ti, Fe, and Ni atoms increases, and they are used to form different intermetallic phases. The peak intensity of the intermetallic phase increases progressively with increasing temperature from 1100 °C to 1200 °C. Elemental Ni was completely used at high temperatures, while Ti and Fe were still present in elemental form. It is observed that the diffusivity rate of Ni is higher than that of other elements. Fe diffusion forms Fe_2Ti , FeTi , and FeNi_3 intermetallics indicating the affinity of Fe towards both Ti and Ni. Fe has a greater tendency to react with Ni than that of Ti (*i.e.*, more FeNi_3 phase is formed than the Fe_2Ti phase). The XRD pattern shows peak intensities of intermetallics increase with an increase in temperature for each of the prepared compositions. The formation of all the phases at the different conditions of this investigation is confirmed by the Ni–Ti, Fe–Ti, and Ni–Fe phase diagrams.^[47] The increase in sintering temperature plays a dominant role in forming stable and metastable phases that are responsible for the densification and hardness of the material. The presence of $\text{NiTi}(\text{B}2)$ and $\text{NiTi}(\text{B}19')$ indicates the shape memory behavior of the prepared composition. The addition of the third element (Fe) yields an intermediate $\text{NiTi}(\text{R})$ phase along the martensite transformation path.^[48] The major peaks of the $\text{NiTi}(\text{R})$ phase are observed in the entire Fe-added sample, whereas a minor peak of the $\text{FeNiTi}(\text{R})$ phase is observed at the 1150 °C sintered sample. These phases are the point of attraction to rise further investigation on NiTiFe alloy to get the shape memory properties.

C. Microstructure Analysis of the Sintered Sample

Figure 4 shows a backscattered SEM image of sintered samples at different sintering temperatures from 1100 °C to 1200 °C. Letters A to I denote different regions (color contrast-wise) in the micrographs, and the corresponding chemical compositions of that region obtained by EDS analysis are given in Table II. Figures 4(a) through (r) shows three distinct phases with varying contrast that can be seen in all the compositions of the alloys prepared at three different temperatures. The white region belongs to the (Ni, Fe)-rich phase, dark region being the β -Ti phase, and the grey region is the α -Ti phase belonging to the Ti-rich phase for all images in Figure 4 and confirmed by EDS analysis of Table II. Ni is the major component in regions B, E, and H for the (Ni, Fe)-rich phase, while Ti is the major component in regions A, D, and G for the α -Ti phase, but region G in Figure 4(i) is the NiTi phase and C, F and I for the β -Ti phase. Detailed EDS analysis was carried out by taking two data points to analyze phase compositions, and small homogeneity variation was seen for the different phases for regions in the microstructure. The change of Ti, Fe, and Ni elements concentration exists between the dark, white, and grey phases. So, the dark and grey phase is richer in Ti and poorer in Ni, and the reverse is true for the white phase. Therefore, from the Figure, it can be concluded that the white region is the (Ni, Fe)-rich phase, and the dark and grey regions are the β -Ti and α -Ti phases. The 4at. pct Fe sample sintered at 1200 °C in Figure 4(i) having matrix phase compositions are NiTi phase, but

all other composition samples sintered at 1200 °C in Figures 4(c, f, l, o, r) and also all composition samples sintered at 1100 °C in Figures 4(a), (d), (g), (j), (m), (p) and 1150 °C in Figures 4(b), (e), (h), (k), (n), (q) having matrix phase are α -Ti phase, as seen from the Figure. It is observed from Table II that with an increase in at. pct Fe, there is a decrease in Ni and Ti amount changes in both phases, *i.e.*, the Ti-rich and (Ni, Fe)-rich phase.

Due to the solid solution of Fe that replaces the Ni atom, such a way that reduces Ni content, and the Fe content increases in both phases. But the “Ni + Fe” to Ti ratio is the same in the TiNiFe alloys. Also, it was observed that the elements Ni and Fe have faster diffusion rates in the α -Ti phase than in the β -Ti phase and the self-diffusion of Ti. The diffusivity of Ni and Fe is the same in Ti, and it increases with increasing

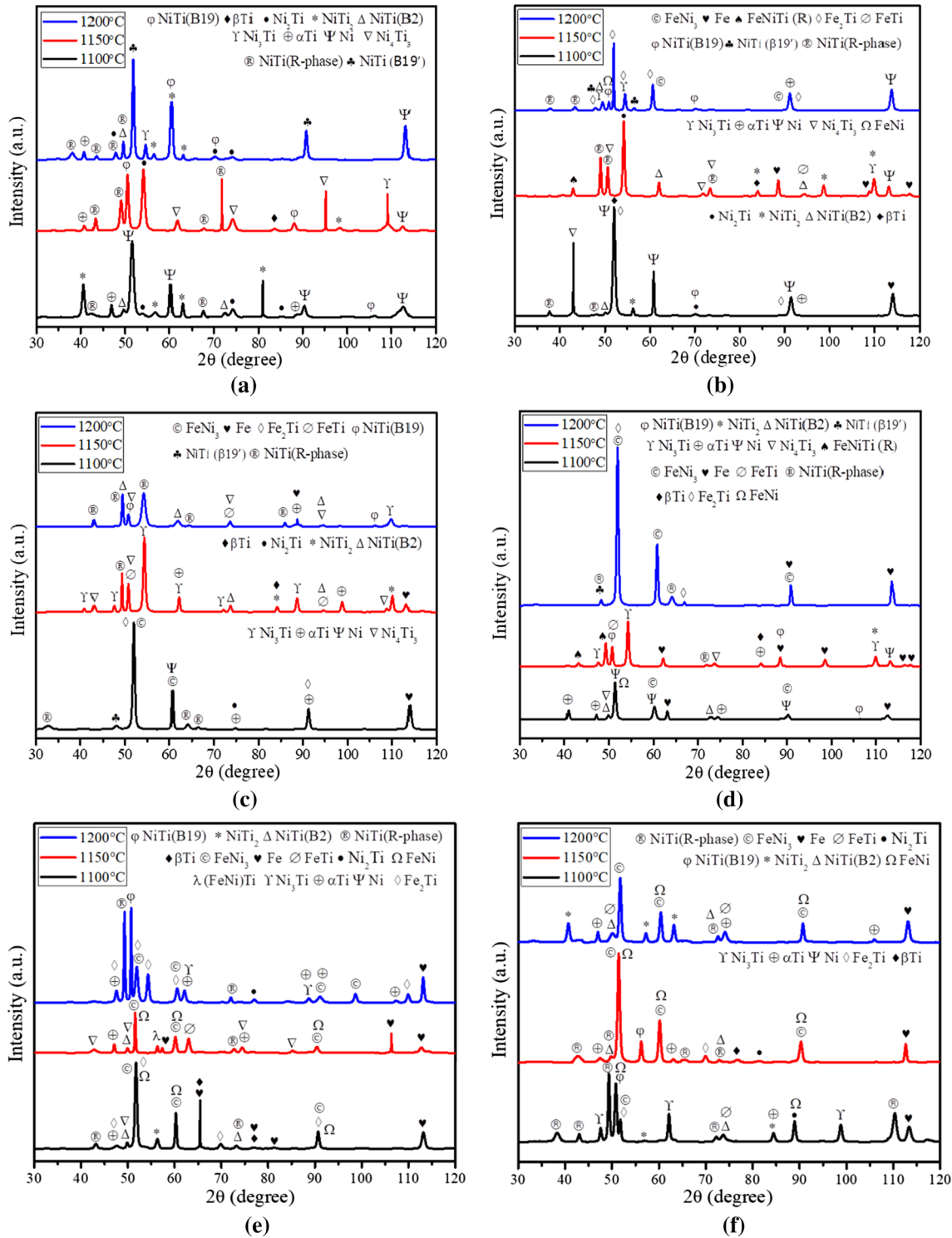


Fig. 3—XRD analysis of (a) 0Fe, (b) 2Fe, (c) 4Fe, (d) 6Fe, (e) 8Fe, and (f) 10Fe samples sintered at different temperatures.

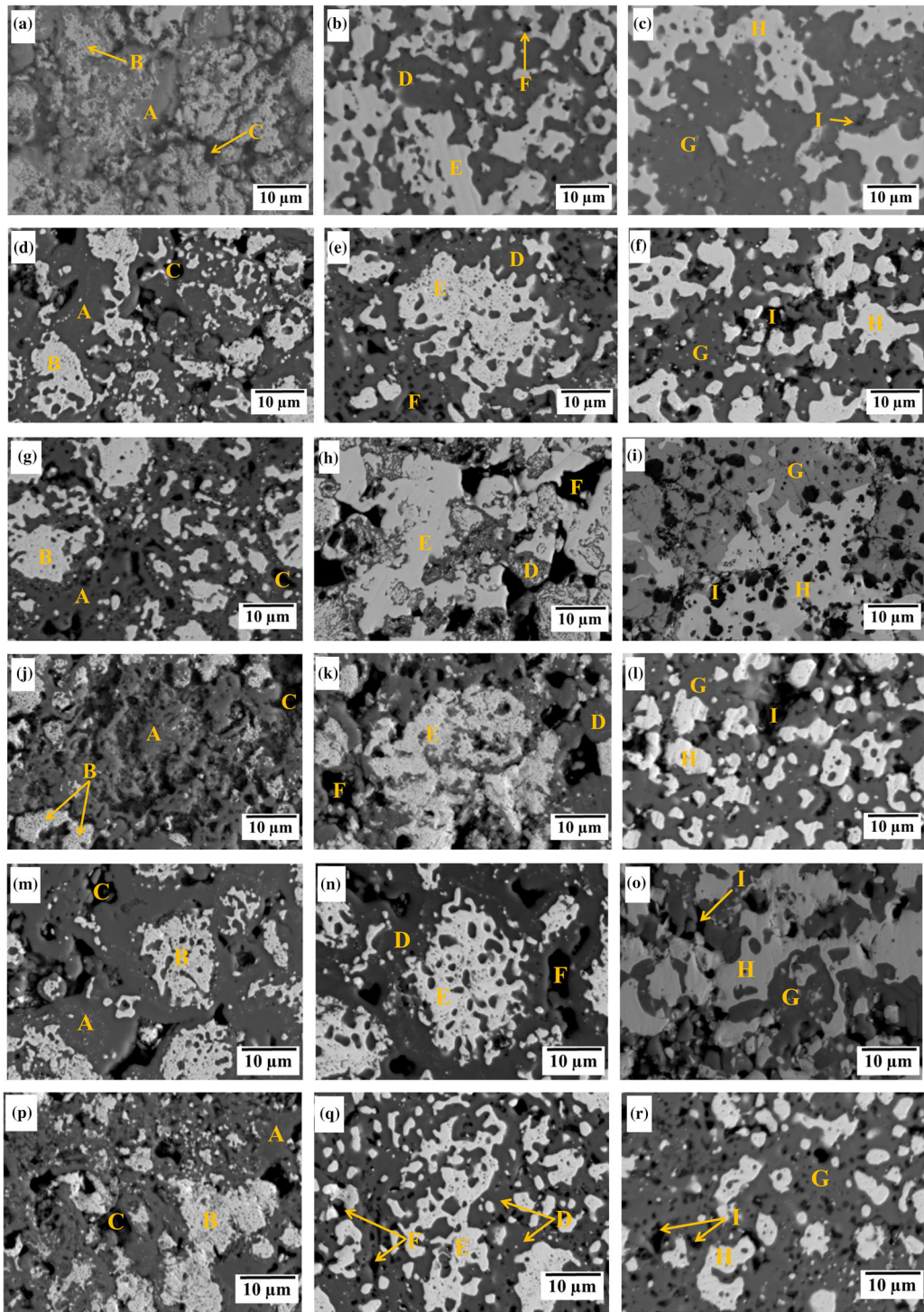


Fig. 4—SEM micrographs of (a, b, c) 0Fe, (d, e, f) 2Fe, (g, h, i) 4Fe, (j, k, l) 6Fe, (m, n, o) 8Fe and (p, q, r) 10Fe samples sintered at different temperatures, *i.e.*, 1100 °C, 1150 °C, and 1200 °C, respectively.

temperature.^[8] Based on the above mechanism, the hardness value is more in α -Ti (matrix phase) phase compared to the β -Ti, as shown in Figure 7(d). Because of the inadequate sintering in TiNiFe alloy sintered at 1100 °C, mainly the pores are gaps between particles. The Kirkendall effect between Ni and Ti shows the voids formed on the Ni side,^[49] and the addition of Fe further

increases the void in the TiNiFe alloy. A more amount of small pores distributed in the alloy sintered at 1100 °C are shown in Table III. With the increase in temperature from 1100 °C to 1200 °C, the pore amount in the TiNiFe alloy significantly decreases, and the pore size increases. At higher temperatures, the additional energy provides stable phase formation that contributes

Table II. EDS Result of the Different Regions or Phases of Samples Sintered at Different Temperatures Placed in Fig. 4

Samples Name	Sintering Temperature	Regions in Micrograph	Composition (At. Pct)				Phase
			Ni	Ti	Fe	Cr	
0Fe	1100 °C	A	35.96	62.97	0.72	0.35	Ti-rich
		B	71.22	27.80	0.83	0.15	Ni ₃ Ti
		C	21.93	76.67	1.06	0.34	Ti-rich
	1150 °C	D	22.23	76.89	0.58	0.30	Ti-rich
		E	69.67	28.71	1.22	0.40	Ni ₃ Ti
		F	32.15	66.16	1.32	0.37	Ti-rich
	1200 °C	G	27.83	70.87	1.02	0.28	Ti-rich
		H	85.30	12.70	1.69	0.31	Ni ₃ Ti
		I	32.72	65.39	1.53	0.36	Ti-rich
2Fe	1100 °C	A	4.30	94.73	0.60	0.37	αTi
		B	80.46	10.83	8.15	0.56	(Ni, Fe)-rich
		C	30.15	65.54	3.73	0.58	Ti-rich
	1150 °C	D	3.60	95.20	0.90	0.30	αTi
		E	88.55	8.98	2.14	0.33	(Ni, Fe)-rich
		F	23.86	74.34	1.39	0.41	Ti-rich
	1200 °C	G	1.98	96.76	0.95	0.31	αTi
		H	81.15	3.28	15.27	0.30	(Ni, Fe)-rich
		I	22.70	62.51	14.56	0.23	Ti-rich
4Fe	1100 °C	A	1.68	97.51	0.51	0.30	αTi
		B	85.60	4.98	9.09	0.33	(Ni, Fe)-rich
		C	6.07	92.69	0.98	0.26	βTi
	1150 °C	D	10.21	87.75	1.88	0.16	αTi
		E	67.70	26.65	5.39	0.26	Ni ₃ Ti
		F	14.61	83.30	1.96	0.13	βTi
	1200 °C	G	27.45	52.64	19.67	0.24	NiTi
		H	65.66	25.00	9.05	0.29	Ni ₃ Ti
		I	1.70	96.77	1.22	0.31	βTi
6Fe	1100 °C	A	1.16	97.68	0.86	0.30	αTi
		B	58.36	17.50	23.87	0.27	(Ni, Fe)-rich
		C	11.79	80.83	7.19	0.19	βTi
	1150 °C	D	2.50	95.66	1.56	0.28	αTi
		E	59.78	32.86	6.99	0.37	Ni ₂ Ti
		F	9.26	85.04	5.48	0.22	βTi
	1200 °C	G	1.78	97.01	0.68	0.53	αTi
		H	77.38	3.11	19.40	0.11	FeNi ₃
		I	30.08	58.34	11.08	0.50	Ti-rich
8Fe	1100 °C	A	1.33	97.80	0.39	0.48	αTi
		B	78.26	3.14	18.14	0.46	(Ni, Fe)-rich
		C	20.49	72.76	6.28	0.47	βTi
	1150 °C	D	1.54	97.46	0.58	0.42	αTi
		E	61.01	13.55	25.15	0.29	(Ni, Fe)-rich
		F	17.39	73.91	8.27	0.43	βTi
	1200 °C	G	1.71	97.84	0.13	0.32	αTi
		H	88.87	3.44	7.30	0.39	(Ni, Fe)-rich
		I	13.99	83.75	1.86	0.40	βTi
10Fe	1100 °C	A	1.01	97.62	1.18	0.19	αTi
		B	70.91	13.13	15.63	0.33	(Ni, Fe)-rich
		C	9.05	88.15	2.55	0.25	βTi
	1150 °C	D	1.32	97.16	1.29	0.23	αTi
		E	44.88	8.81	45.81	0.50	(Ni, Fe)-rich
		F	8.82	89.43	1.49	0.26	βTi
	1200 °C	G	2.10	96.70	1.01	0.19	αTi
		H	72.43	3.87	23.43	0.27	FeNi ₃
		I	7.00	91.09	1.55	0.36	βTi

to better hardness and densification by decreasing porosity.

Figures 5 and 6 represent line scan analysis and elemental mapping of the 4Fe sample sintered at 1100 °C, respectively. Figures 5(a) and (b) represents a

line scan analysis of the sample in the form of a yellow line. When we compare the three phases, it is seen that the amount of Ni and Fe is more in the white phase, and Ti is more in the dark and grey phases. From this, we confirmed that the white phase belongs to the (Ni,

Table III. Relative Densities Considering Without and with the Internal Pores and Porosity Percentage for Samples Sintered at Different Temperatures

Sample Name	Sintering Temp	Rel. Density (Only External Pores Considered) (Pct)	Rel. Density (Both External and Internal Pores Considered) (Pct)	Porosity (Pct)
0Fe	1100 °C	66.398	55.077	17.05
	1150 °C	66.674	55.525	16.72
	1200 °C	71.475	58.979	17.48
2Fe	1100 °C	63.40	48.659	23.26
	1150 °C	70.359	59.079	16.03
	1200 °C	77.807	65.382	15.97
4Fe	1100 °C	64.729	50.978	21.24
	1150 °C	79.255	67.162	15.26
	1200 °C	81.422	69.244	14.96
6Fe	1100 °C	65.438	52.144	20.32
	1150 °C	66.913	55.484	17.08
	1200 °C	74.734	62.424	16.47
8Fe	1100 °C	75.656	63.54	16.02
	1150 °C	66.731	55.196	17.29
	1200 °C	74.21	61.703	16.85
10Fe	1100 °C	66.173	53.831	18.65
	1150 °C	66.726	55.065	17.48
	1200 °C	73.781	61.173	17.09

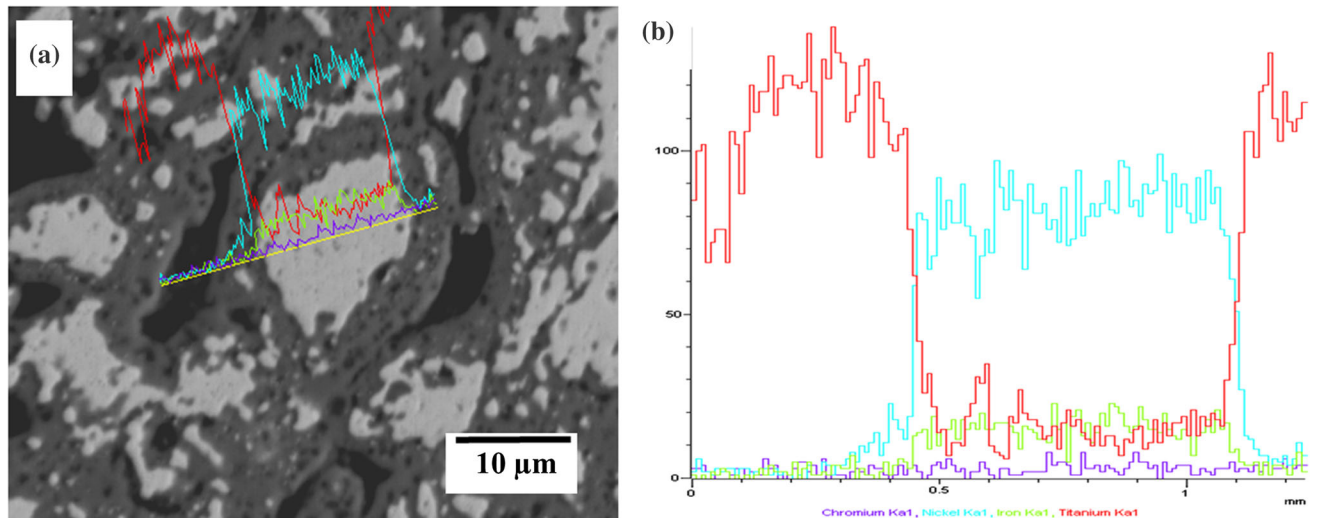


Fig. 5—Line scan analysis of the 4Fe sample sintered at 1100 °C for change in concentration of Ni, Ti, Fe, and Cr elements with respect to a different phase.

Fe)-rich phase, and the dark and grey phase is the Ti-rich phase. From Figures 6(a) through (e), we see that different elements like Fe, Ti, Cr, and Ni are uniformly distributed in the micrograph of the sample. It confirms that the (Ni, Fe)-rich phase belongs to a white phase that consists of Ni and Fe elements for samples, which implies Ni_3Ti , Ni_2Ti , and Fe_3Ti , etc. The Ti-rich phase belongs to the dark and grey phase consisting of Ti elements in the sample, which implies α -Ti and β -Ti. The Cr element present in few

percentages in the sample is due to the milling media, *i.e.*, stainless steel balls and vial.

D. Densification Analysis of the Sintered Sample

1. Porosity determination

During the sintering process, unavoidable components, *i.e.*, pores, are produced in the microstructure of the sample. They are of two types: (a) open pores in which pores are contacted with the outer surface of the

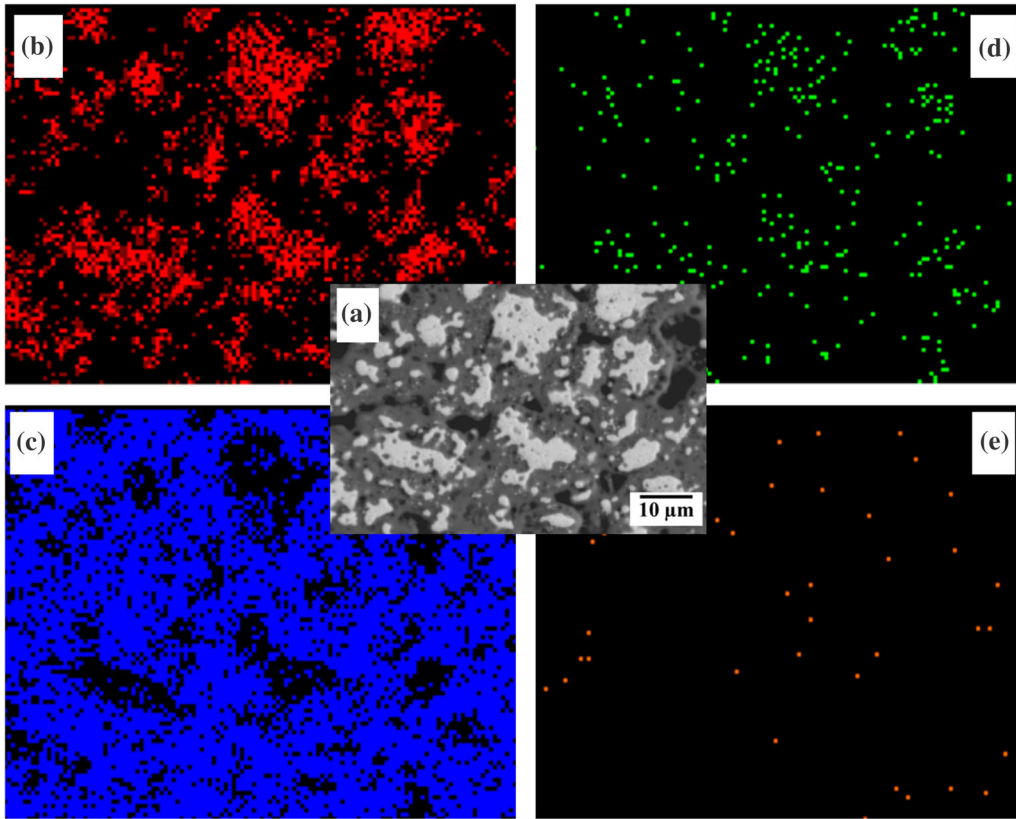


Fig. 6—Elemental mapping of a 4Fe sample sintered at 1100 °C: (a) Backscattered SEM image, (b) Ni, (d) Fe, (c) Ti, and (e) Cr.

sample (Case I), and (b) closed pores in which pores are gaps between particles (Case II). Generally, pore diameter depends on sintering conditions and particle size. As per the Archimedes principle, the following Eqs. [2] and [3] are used for density and porosity calculations in both cases.^[50–52]

$$\text{Case I: Density of sample} = \frac{m_1}{m_1 - m_2} \times \rho_w \quad [2]$$

$$\text{Case II: Density of sample} = \frac{m_1}{m_3 - m_2} \times \rho_w \quad [3]$$

where m_1 = mass of the sample in air, m_2 = mass of the sample in submerged water, m_3 = soaked mass of the sample after 24 h in distilled water, and ρ_w = density of water. The relative density of the sample is a lower value when considering both external pores (surface open pores) and internal pores (closed pore and internal interconnected pore). If only external pores are considered, then the density values are between 63 and 81 pct, as shown in Table III. The total pore or apparent porosity pct can be calculated by Eq. [4]:

$$\text{Apparent porosity (\%)} = \frac{m_3 - m_1}{m_3 - m_2} \times 100 \quad [4]$$

For the 1100 °C sintering temperature, the porosity for the 2 at. pct Fe sample is 23.26 pct, and this value decreases from 16.03 to 15.97 pct with increasing the

sintering temperature from 1150 °C to 1200 °C. Similarly, the porosity values decrease with temperature for other composition samples. The porosity value decreases significantly at 1200 °C due to more inter-diffusion, which helps more pores be eliminated from the sample^[53] and provides higher density, hardness, and better mechanical properties. Fe addition helps with easier diffusion and is responsible for densification enhancement by closing the internal pores through particle rearrangement. The 8 at. pct Fe sample sintered at 1100 °C shows a lower value of porosity is 16.02 pct, compared to other composition samples. Due to this reason, the 8 at. pct Fe sample shows better properties than other compositions. Similarly, the 4 at. pct Fe samples sintered at 1150 °C and 1200 °C show a lower value of porosity of 15.26 and 14.96 pct, respectively, compared to other compositions and other sintering temperatures. The reason for changes in porosity values is due to the formation of necks between powder particles with respect to the provided temperature. That neck formation is responsible for initiating surface-to-surface atom migration and grain-boundary volumetric diffusion that results in a densification mechanism.^[54]

2. Density measurement

Figure 7 shows the experimental and relative densities values of all composition samples sintered at different temperatures. The experimental and relative densities of a sintered sample are shown in Figure 7(a). The relative

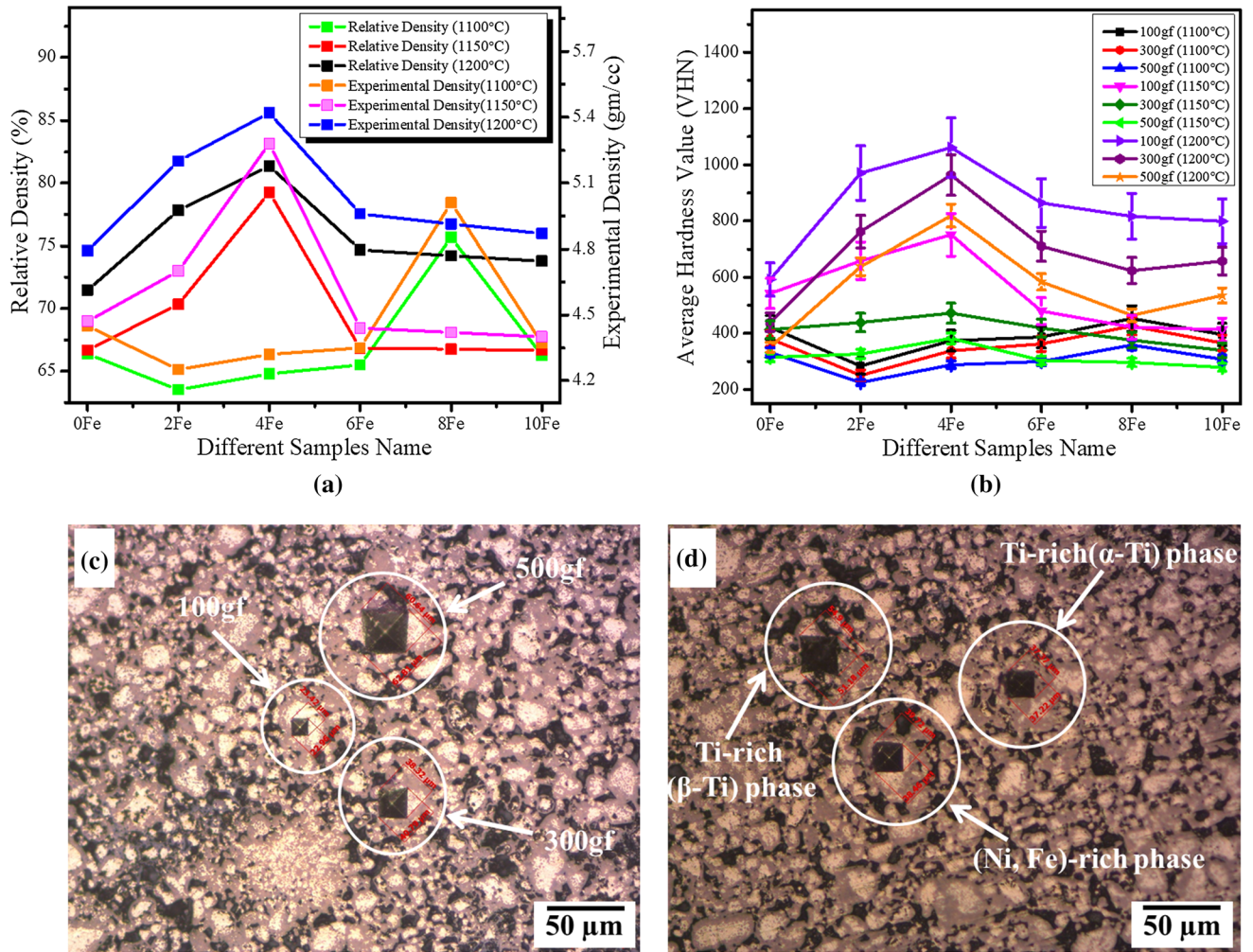


Fig. 7—(a) Relative and Experimental density, (b) Indentation load effects (100, 300, and 500 gf) on the hardness values of 0Fe, 2Fe, 4Fe, 6Fe, 8Fe, and 10Fe samples sintered at different temperatures, and an optical image of (c) load indentation effect on the sample surface and (d) load indentation on different phases on the surface of a sample.

and experimental density of the sample are calculated by the Archimedes principle using the following Eqs. [5] and [6].^[19]

$$\text{Experimental density (g/cc)} = \frac{m_1}{m_2 - m_3} \times \text{water density}, \quad [5]$$

where m_1 = initial sample mass in air, m_2 = soaked sample mass in air, and m_3 = soaked sample mass in distilled water.

$$\text{Relative density (\%)} = \frac{\text{Experimental density}}{\text{Theoretical density}} \times 100 \quad [6]$$

It was found that sintered at 1200 °C sample resulted in higher density values than the sample sintered at 1100 °C and 1150 °C. For the density value of all composition samples sintered at 1100 °C, it is found that density value increases from 2 to 8 at. pct Fe (with an increasing Fe percentage) and maximum value at 8 at. pct Fe is 75.26 pct and then decreases at 10 at. pct Fe.

But in the case of samples sintered at 1150 °C and 1200 °C, the maximum density value found at 4 at. pct Fe is 79.26 and 81.36 pct, respectively, than other composition samples. If we compare samples of all three sintering temperatures, it is found that 4 at. pct Fe at 1200 °C has the maximum density value and 2 at. pct Fe at 1100 °C has the minimum density value compared to other sintering temperatures and composition samples because higher density is achieved due to full densification of the sample. For the samples sintered at 1100 °C, there are many un-sintered particles observed (*i.e.*, insufficient diffusion takes place). By increasing the temperature to 1150 °C, an improvement in densification is observed, and at 1200 °C temperature, the fully sintered surface without an undiffused particle is observed. This is confirmed by the SEM analysis in Figure 4. These results indicate that the enhancement of densification during sintering occurs at a temperature of 1100 °C to 1200 °C. So, density values increase with increasing sintering temperature due to enhanced diffusion bonding with increased temperature. In addition, the porosity amount is more at the lower sintering

temperature, *i.e.*, 1100 °C, and decreases with increased sintering temperatures from 1150 °C to 1200 °C because the porosity percentage is inversely proportional to relative density or experimental density value.

E. Hardness Measurement of the Sintered Sample

The hardness value of all the densified samples can be found using Vickers micro-hardness test by the following Eq. [7]^[55]:

$$HV = 1.8544 \frac{F}{d^2}, \quad [7]$$

where F is the indentation load and d is the indentation diagonal length.

The average hardness value changes for all the samples with respect to different applied loads, as shown in Figure 7(b). The average hardness value increases with decrease in applied load because of indentation elastic recovery and smaller size indentation at lower loads^[56] or due to the indentation size effect (*i.e.*, surface effect and strain gradient effect).^[57] The hardness values of the sample are determined based on the indentation depth, which is inversely proportional to hardness.^[58] Therefore, with the increase in applied load from 100 to 500 gf, the indentation depth increase, and thus, the hardness values decrease, as shown in Figure 7(c). Also seen from the experiment, the hardness values change in the different regions at a constant load due to compositional heterogeneity or various phases in Figure 7(d). The Figure shows that the hardness values of without-Fe and with-Fe (8 at. pct Fe) sintered at 1100 °C are 381.2 and 426.2 VHN, respectively. The 8 at. pct Fe sample has a higher hardness value compared to other composition samples from 2 to 10 at. pct Fe and also from 0 at. pct Fe (without-Fe) because of the formation of more intermetallic phases and the presence of $\text{Fe}_2\text{Ti} + \text{FeNi}_3$ as a major or secondary phase after the addition of iron, as well as its higher density (lower porosity), which helps for higher hardness. The maximum hardness value seen in a 4 at. pct Fe sample is 472.1 and 963.3 VHN, respectively, when the samples are sintered at 1150 °C and 1200 °C due to the presence of Ni_4Ti_3 intermetallic as a major or secondary phase. When we compare the hardness values of all sintering temperatures and all composition samples, it is seen that at 4 at. pct Fe sintered at 1200 °C shows higher densification than other composition samples because of their higher density (less number of voids). Also increased sintering temperature from 1100 °C to 1200 °C, the hardness and densification value of all samples increased significantly due to the solid solution of Fe in the matrix and the increase in the $\text{Ti}_2\text{Ni}/\text{Fe}_2\text{Ti}/\text{FeNi}_3$ strengthening phase amount or presence as a major or secondary phase and substitution strengthening of the NiTi/FeTi phase which helps to the increase of the hardness value.^[19] Therefore, the increased hardness value of samples is due to two reasons: (a) higher densification due to higher density, and (b) the presence of stable phases and precipitates, which can strengthen the matrix.^[59]

F. Compressive Strength of the Sintered Sample

Figure 8(a) and (b) shows the true stress–strain curve of all samples sintered at 1100 °C and 1150 °C, and Figure 8(c) shows the variation of compressive strength, yield strength, and elastic modulus with respect to different samples. Figure 8(a) shows the 8 at. pct Fe sample that gives the maximum true stress value due to being capable of taking more stress compared to other composition samples, but the 0 at. pct Fe sample shows the maximum true strain value due to good plasticity compared to other composition samples sintered at 1100 °C. Figure 8(b) shows the 4 at. pct Fe samples sintered at 1150 °C that give the maximum true stress value, but the 8 at. pct Fe sample shows the maximum true strain value compared to other composition samples. The reason behind the maximum true stress value of the sample is the formation of more intermetallic phases with respect to the addition of Fe contents and fully sintered (achieving higher density and lower porosity) at that same sintering temperature of the sample compared to other compositions. During compressive loading, this intermetallic phase is capable of bearing the load and showing a better true stress value. Also, significant fluctuation is seen in the stress–strain curve because during loading, the contact between particles is broken, and the strength decreases. Again, immediately the other particles bear that load up to their breaking point, so the strength is again increased. In this way, each and every particle has to bear the load up to the breaking of all the particles. But in the case of 1150 °C, the densification is more than that of 1100 °C, and the effect of the NiTi shape memory behavior is more which gives more compressive stress compared with the less densified sample. Figure 8(c) shows all three values (compressive strength, yield strength, and elastic modulus), in which the values are higher for the 8 at. pct Fe sample of 62.65 MPa, 56.11 MPa, and 10.1 GPa, respectively, that were sintered at 1100 °C, whereas for 4 at. pct Fe sample sintered at 1150 °C having the values were 132.57 MPa, 116.86 MPa, and 11.96 GPa, respectively. When comparing both strength and elastic modulus of all samples prepared at both temperatures shows 4 at. pct Fe sample sintered at 1150 °C has higher values of compressive strength, yield strength, and elastic modulus is 132.57 MPa, 116.86 MPa, and 11.96 GPa, respectively, compared to other composition samples. The reason behind higher values is that the diffusion of elemental atoms was sufficient for the formation of intermetallic compounds and sintering necks between different particles, resulting in a lower porosity value with better densification.^[18] All three values increase for all composition samples with the increase in sintering temperature from 1100 to 1150 °C due to the increase in densification. Hence, the strength and elastic modulus increase with an increase in sintering temperature.^[60] Based on Zhu *et al.*,^[61] increase in sintering temperature helps to improve the atomic diffusion and strengthen the material. But the 0 at. pct Fe and 6 at. pct Fe samples show a decrease in strength and elastic modulus with an increase in sintering temperature because the sample is unable to

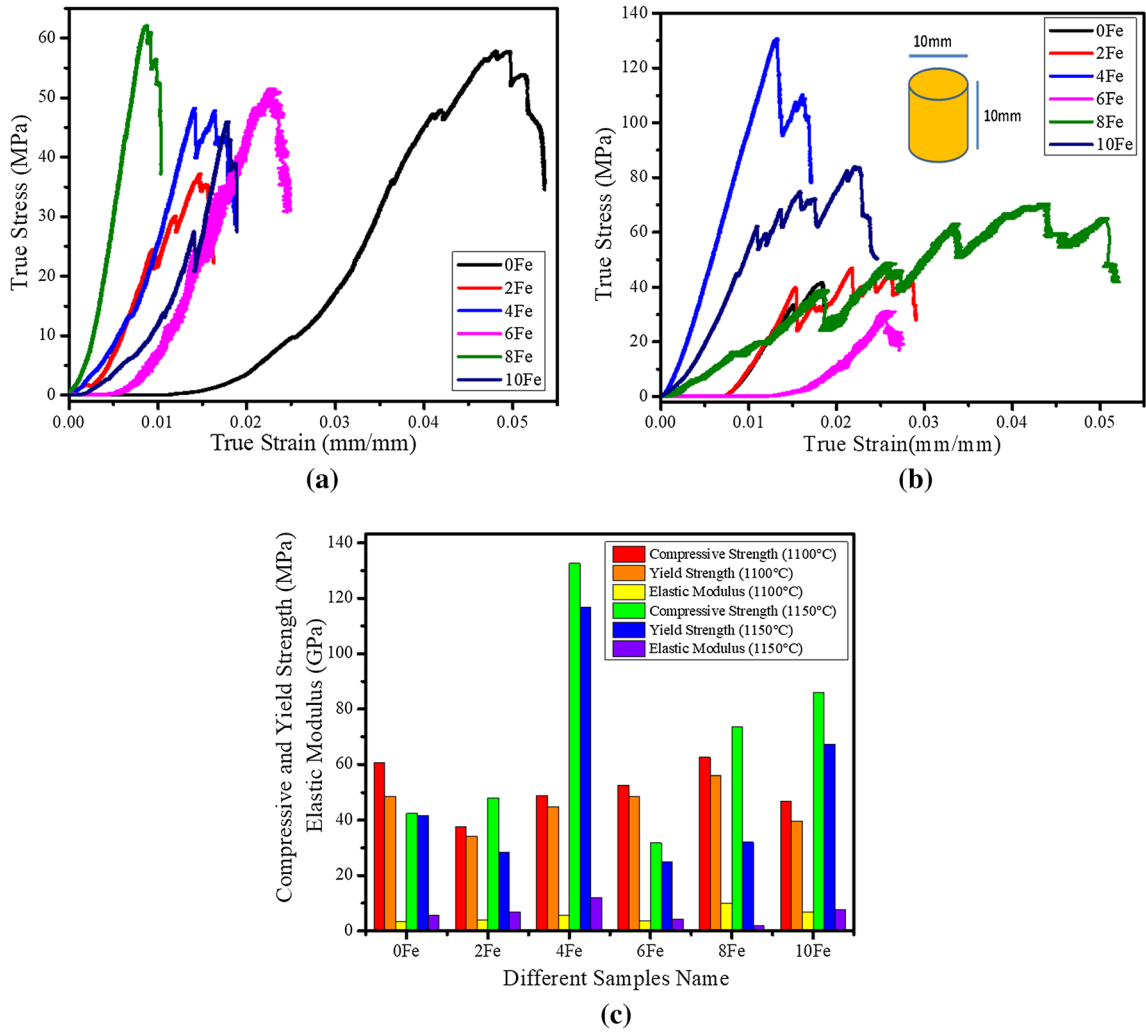


Fig. 8—True stress vs true strain curve of (a) 1100 °C, (b) 1150 °C samples (dimension of sample is put in the inside graph), and (c) Maximum compressive strength, yield strength, and elastic modulus value of 0Fe, 2Fe, 4Fe, 6Fe, 8Fe and 10Fe samples sintered at 1100 °C and 1150 °C temperatures, respectively.

resist further loading beyond that hardness value due to brittle behavior. The porosity amount of the 4 at. pct Fe sample sintered at 1150 °C is 15.26 pct, which is lower than other composition samples. Therefore, it provides a better compressive and yield strength value than other composition samples. Similarly, the porosity amount of the 8 at. pct Fe sample sintered at 1100 °C is 16.02 pct. So, it shows a better compressive and yield strength value compared to other composition samples. The main reason for the better compressive strength is the higher load-bearing area of the sample with a decrease in porosity.^[61]

G. Wear Behavior of the Sintered Sample

The wear behavior of the surface has been analyzed by the sliding wear test for all the samples. Figures 9(a), (c), (e) and (b), (d), (f) represent the variation in wear depth and friction coefficient with sliding distance for samples sintered at 1100 °C, 1150 °C, and 1200 °C, respectively. Equations (8) and (9) are used to determine

sliding distance^[62] and friction coefficient^[63] in the sliding wear analysis;

$$\text{Sliding Distance} = \frac{R}{60} * t * 2\pi r \quad [8]$$

$$\text{Friction coefficient}(\mu) = \frac{F}{N}, \quad [9]$$

where R is the number of times the ball revolves per minute on a sample surface, t is the time (sec), r is the track radius (mm), F is the frictional force, and N is the applied load. The friction coefficient is a measurement of frictional force, which is related to the amount of damage/debris formed on the surface. When the frictional force is extremely low, the friction coefficient is also extremely low, and no permanent damage occurs on the surface. However, with increasing frictional force, more damage will be induced during the wear test; hence the friction coefficient will be increased.^[33]

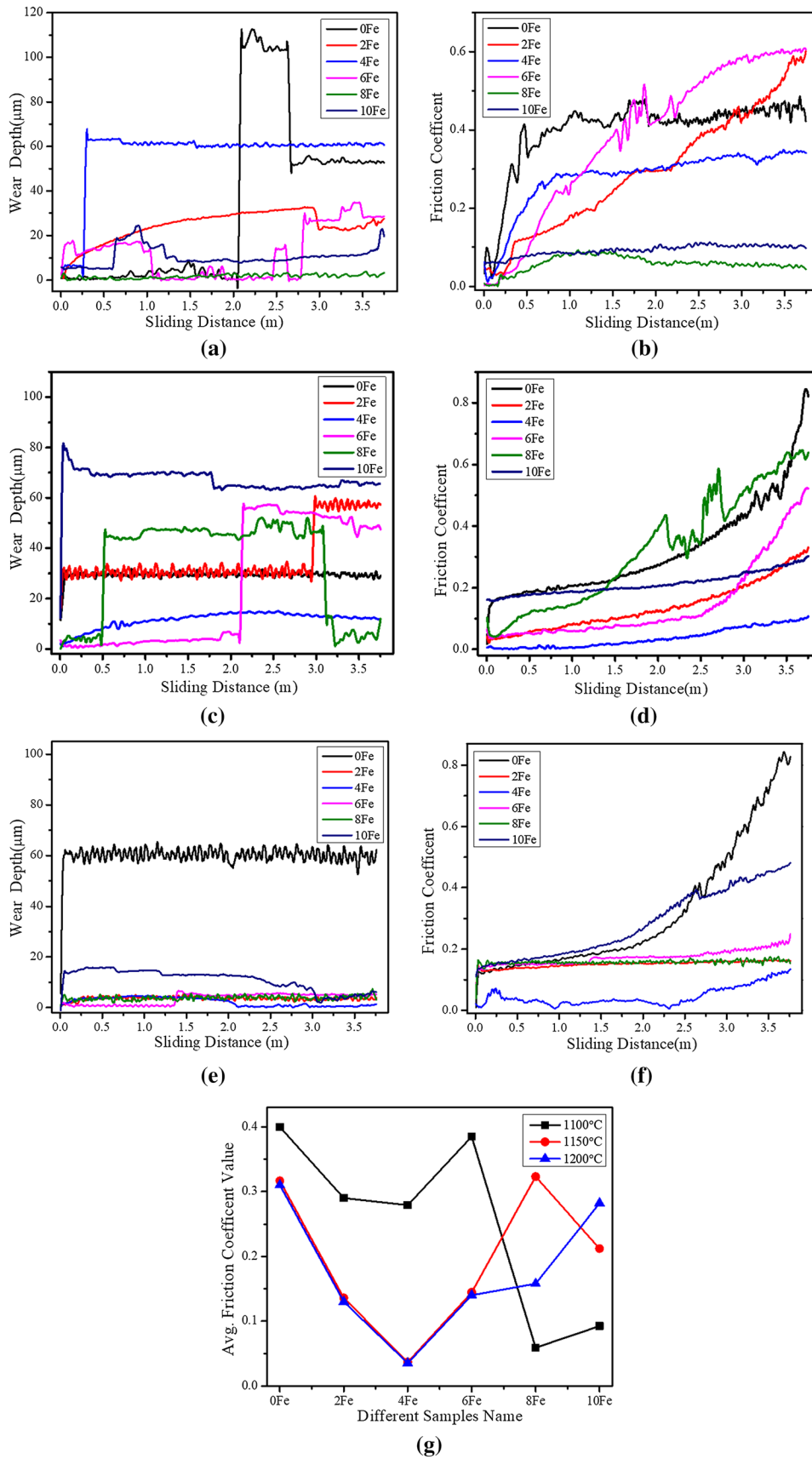


Fig. 9—(a, c, e) Wear depth, (b, d, f) Friction coefficient vs sliding distance, and (g) Average friction coefficient value vs different samples name sintered at different temperatures.

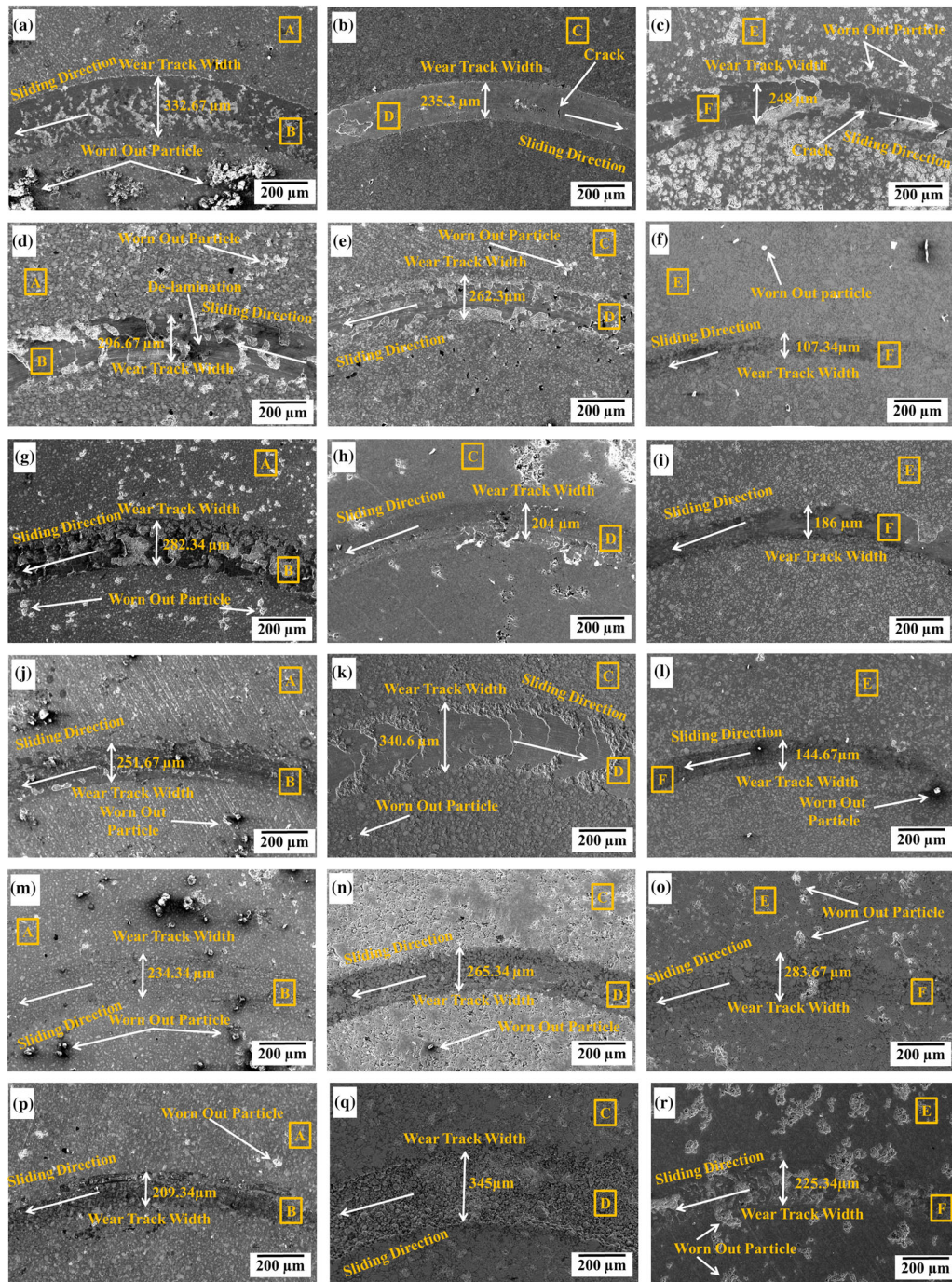
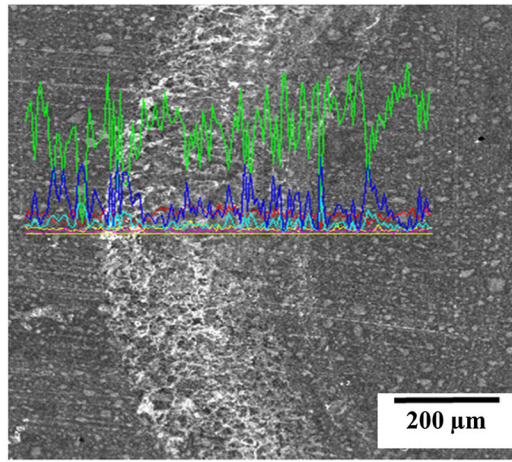


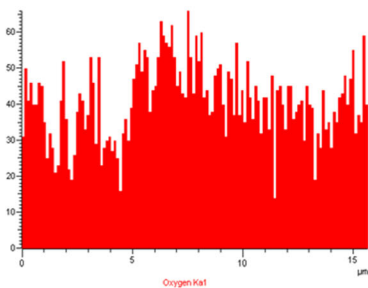
Fig. 10—Worn surface analysis of (a, b, c) 0Fe, (d, e, f) 2Fe, (g, h, i) 4Fe, (j, k, l) 6Fe, (m, n, o) 8Fe and (p, q, r) 10Fe samples sintered at different temperatures.

The friction coefficient value of 0.06 was found in the 8 at. pct Fe sample sintered at 1100 °C, which is lower than other composition samples for the same sliding distance and load. Similarly, the lower friction coefficient obtained for the 4 at. pct Fe sample sintered at 1150 °C and 1200 °C is 0.037 and 0.035, respectively, than other composition samples, as shown in Figure 9(g). Based on the literature, a higher elastic modulus value is responsible for a lower friction coefficient.^[37] The elastic modulus values of 4 at. pct

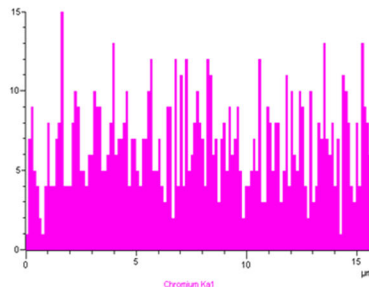
Fe and 8 at. pct Fe samples sintered at 1150 °C and 1100 °C, respectively, are 11.96 and 10.01GPa, which are higher than other composition samples. If we compare three sintering temperature samples, the 4 at. pct Fe sample at 1200 °C has a lower friction coefficient (0.035) compared to other compositions and other sintering temperature samples. So, the friction coefficient value decreases with an increase in temperature from 1100 °C to 1200 °C due to the formation of hard secondary phase particles, higher hardness (much lower



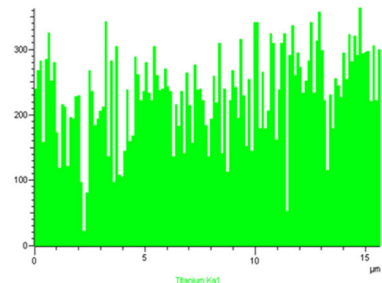
(a)



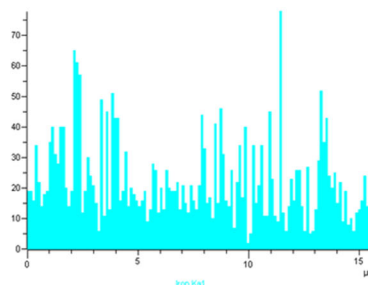
(b)



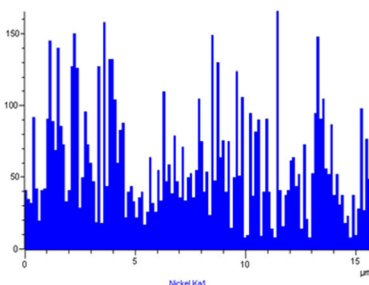
(c)



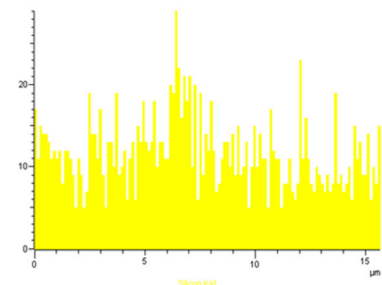
(d)



(e)



(f)



(g)

Fig. 11—(a) The line scan analysis of the worn surface of the sample with respect to variation of the element is (b) O, (c) Cr, (d) Ti, (e) Fe, (f) Ni, and (g) Si.

ductility), density, and elastic modulus values.^[37,64] In addition, Fe addition helps lower the friction coefficient and minimum wear depth of the sample shown in Figures 9(a) through (f) because of the higher density and hardness value of the samples. Therefore, a higher sintering temperature and Fe addition help enhance the wear resistance or abrasion behavior of an alloy sample. When the sintering temperature increases from 1150 °C to 1200 °C, the friction coefficient value of the sample decreases. The rapid increase in friction coefficient shows the damage in the matrix phase, debris formation, and material loss. These results indicate an improvement in the wear resistance of the sample. Wear performance

for NiTi-based alloys depends on the unique superelasticity and shape memory effect.^[65] The higher is the densification, the higher is the shape memory behavior, and the lower is the surface damage.

Figure 10 represent SEM images of the worn surfaces of samples sintered at 1100 °C, 1150 °C, and 1200 °C, respectively. SEM-equipped EDS has investigated the worn surface morphology and wear debris produced to study the associated wear mechanisms. Generally, the delamination mechanism in the surface layer shows more material removed from the surface during abrasive wear. However, microcracking and subsequent fracture on the surface layers of the sample results in less

Table IV. EDS Analysis of Sample Chemical Compositions of Wear Track (B, D and F) and Outside Wear Track (A, C, and E) Regions Sintered at 1100 °C, 1150 °C, and 1200 °C are Marked in Fig. 10

Samples Name	Sintering Temp	Phase Regions	Composition (at. pct)					
			Ni K	Ti K	Fe K	Cr K	Si K	O K
0Fe	1100 °C	A	22.23	34.23	0.85	0.39	—	42.30
		B	28.92	26.81	1.08	0.32	1.02	41.85
	1150 °C	C	25.14	32.97	1.03	0.44	—	40.42
		D	26.03	30.99	1.11	0.46	1.10	40.31
	1200 °C	E	23.06	33.47	1.11	0.47	—	41.89
		F	25.64	30.03	0.83	0.33	0.98	42.19
2Fe	1100 °C	A	25.76	24.54	2.48	0.38	—	46.84
		B	23.84	27.55	1.67	0.29	0.87	45.78
	1150 °C	C	24.07	31.42	4.63	0.21	—	39.67
		D	21.75	29.29	4.62	0.44	1.01	42.89
	1200 °C	E	23.94	32.53	1.92	0.41	—	41.20
		F	24.92	30.98	1.61	0.31	0.91	41.27
4Fe	1100 °C	A	22.32	33.05	1.57	0.14	—	42.92
		B	22.48	28.88	1.56	0.20	1.24	45.64
	1150 °C	C	26.40	24.90	4.67	0.30	—	43.73
		D	24.20	21.88	3.51	0.28	1.53	48.60
	1200 °C	E	20.62	28.91	1.92	0.36	—	48.19
		F	22.85	30.57	1.49	0.21	1.80	43.08
6Fe	1100 °C	A	20.41	27.42	4.02	0.22	—	47.93
		B	24.80	28.16	2.42	0.19	0.74	43.69
	1150 °C	C	19.66	25.95	7.06	0.47	—	46.86
		D	21.60	29.73	5.13	0.42	0.98	42.14
	1200 °C	E	17.48	27.96	5.85	0.45	—	48.26
		F	19.55	20.55	5.56	0.43	0.88	53.03
8Fe	1100 °C	A	19.47	34.37	3.12	0.24	—	42.80
		B	21.05	32.48	3.11	0.14	1.39	41.83
	1150 °C	C	19.77	34.06	3.71	0.44	—	42.02
		D	19.64	29.69	3.34	0.48	0.71	46.14
	1200 °C	E	21.59	26.42	6.58	0.14	—	45.27
		F	18.92	23.82	6.76	0.12	0.86	49.52
10Fe	1100 °C	A	17.05	33.76	4.44	0.24	—	44.51
		B	18.40	20.13	9.07	0.16	1.07	51.17
	1150 °C	C	18.55	27.71	8.93	0.37	—	44.44
		D	20.47	24.28	6.92	0.34	1.02	46.97
	1200 °C	E	23.36	24.98	6.06	0.17	—	45.43
		F	15.97	23.26	5.72	0.24	0.90	53.91

material removal. In addition, material removal is higher in a few samples due to predominant brittle fractures and softer surface layers. The micro-cracks formed in some areas of the worn surface, as shown in Figures 10 (b) and (c), and the delamination mechanism governed the wear behavior of the sample. The delamination takes place at a sample of low hardness value sintered only at 1100 °C, shown in Figure 10(d). According to Archard's equation, the wear debris removal amount from the sample surface depends on the hardness of the sample and sintering temperature (*i.e.*, the higher the hardness value and increased sintering temperature, the lower the wear debris amount removal). In some parts of the worn surfaces, the detached wear debris was cold-welded to the worn surface due to the repeated motion of the ball, and other wear debris that was removed from the worn surface was carried out to the near outside worn surface during the wear test, as shown in Figure 10. The enhanced wear resistance of the sample is observed in the Fe-added

sample as compared to the without-Fe sample due to the hindrance of dislocation motion caused by the presence of hard intermetallic particles after sliding or deformation and the extension of plastic deformation. Also, wear track width is more in the Fe-containing sample as compared to the Fe-less sample. For each sample, track widths are taken in the three different areas, and the average value is reported in Figure 10.

When we compare all samples sintered at 1100 °C, the 8 at. pct Fe sample shows a lower worn surface, and 0 at. pct Fe shows a higher worn surface. It confirmed that the 8 at. pct Fe sample shows higher wear resistance compared to others, as shown in Figures 10(a), (d), (g), (j), (m), (q). Similarly, both 4 at. pct Fe samples show a lower worn surface that sintered at 1150 °C and 1200 °C compared to other composition samples. Among the 1200 °C sintered sample, the 4at pct Fe sample gives lower damage to the surface, as shown in Figure 10(i). The reason behind lower damage to the worn surface (*i.e.*, higher resistance of surface ability with respect to

sliding wear) is due to the presence of a hard intermetallic phase (which provides a protective layer for improving load-carrying ability) and shape memory phases that yields improve densification, higher hardness, and strength.^[62]

Figure 11 shows a line scan analysis of the worn surface of the sample to detect the effect of various elements on the worn surface. Figure 11(a) shows that

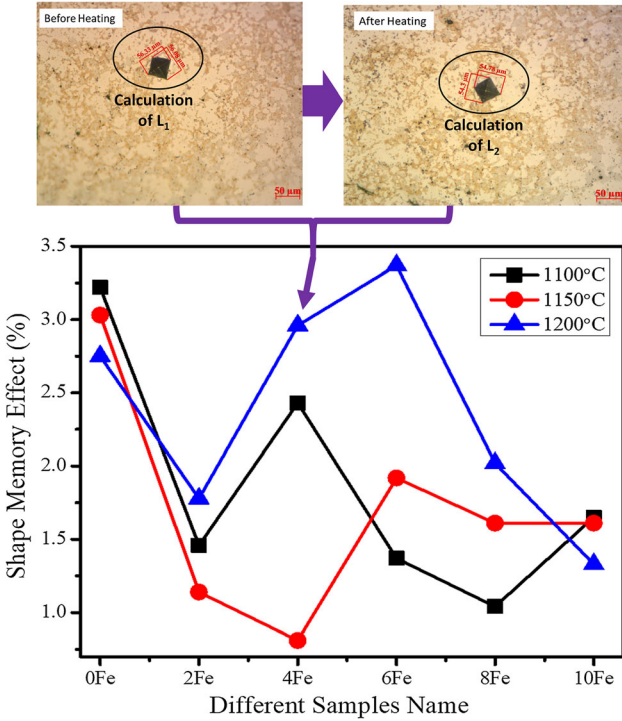


Fig. 12—Shape memory effect percentages of 0Fe, 2Fe, 4Fe, 6Fe, 8Fe, and 10Fe samples sintered at different temperatures along with the topography of an indentation before and after heating.

the line scan draws through the worn surface from one side to the other. The oxygen and silicon intensity are high on the worn surface compared to the without-worn surface, whereas Ni, Ti, and Fe amounts are low on the worn surface compared to the without-worn surface, as shown in Figures 11(b) through (g). The silicon element present in the worn surface comes from the ceramics Si₃N₄ ball due to abrasion occurring between the ball and sample surface. The results indicated that the amount of Si value reached 1.39, 1.53, and 1.80 pct for the sample of 8 at. pct Fe at 1100 °C, and all 4 at. pct Fe sintered at 1150 °C, and 1200 °C, respectively, which indicates the higher wear resistance of this sample as shown in Table IV. In this sample, abrasive wear is the primary mechanism due to the difference in hardness between the ball and the sample surface.^[42] In addition, the presence of oxygen indicates the formation of an oxide layer on the worn surface.

H. Shape Memory Behavior of the Sintered Sample

The following Eq. [1] calculates the shape memory effect percentage for each of the sintered samples, as shown in Figure 12. The average deformed diameter of L₁ and thermal energy stimulated diameter of L₂ for each sample have been calculated and given in Table V. For the 2Fe sample, the SME percentage is minimum, indicating that less percentage of Fe is insufficient to form the shape memory intermetallic and forms metastable phases. By increasing the Fe percentage from 4 at. pct to 6 at. pct, the recovery percentage increases significantly, whereas, with a further increase in the Fe percentage to 8 at. pct and 10 at. pct, there is a decrease in the SME percentage. By increasing the sintering temperature, the same trend can be found (minimum recovery percentage present in 2 at. pct Fe, gradually increasing up to 6 at. pct Fe, and then

Table V. SME Properties of All Composition Samples

Sample name	Sintering temp	L ₁ (μm)	L ₂ (μm)	SME (Pct)
0Fe	1100 °C	121.685	117.77	3.22
	1150 °C	94.115	91.265	3.03
	1200 °C	71.145	69.19	2.75
2Fe	1100 °C	135.925	133.945	1.46
	1150 °C	143.33	141.69	1.14
	1200 °C	91.79	90.16	1.78
4Fe	1100 °C	195.185	190.435	2.43
	1150 °C	360.72	357.785	0.81
	1200 °C	56.205	54.54	2.96
6Fe	1100 °C	210.715	207.835	1.37
	1150 °C	177.54	174.125	1.92
	1200 °C	90.63	87.58	3.37
8Fe	1100 °C	135.025	133.615	1.04
	1150 °C	156.675	154.15	1.61
	1200 °C	70.175	68.755	2.02
10Fe	1100 °C	125.64	123.57	1.65
	1150 °C	185.66	182.665	1.61
	1200 °C	75.795	74.785	1.33

decreasing in 8 at. pct Fe and 10 at. pct Fe). It is found that 0Fe samples sintered at 1100 °C and 6Fe samples sintered at 1200 °C show maximum SME percentages of 3.22 pct and 3.37 pct, respectively. The higher diffusion favors better densification, which yields a more stable NiTi (B19' and B19) phase in the sample.^[66] It is proven that, as per the analysis, 1200 °C is the optimum sintering temperature to get a better SME percentage with the 6 at. pct Fe. In 6 at. pct Fe, the hard anti-SME NiTi₂ phase is absent, and a minor percentage of SME favored FeNiTi(R) phase is present. The effect of other phases such as Ni₃Ti, Ni₄Ti₃, NiTi₂, Ni₂Ti, FeTi, FeNi, Fe₂Ti, and FeNi₃ has not been analyzed so far for shape memory behavior. However, they are also responsible for mechanical strength and wear resistance.

IV. CONCLUSIONS

The conclusions derived from the microstructure, phase analysis, and physical and mechanical properties of the sintered TiNiFe alloy samples are as follows:

- i. SEM and XRD analyses of samples sintered at 1100 °C to 1200 °C consist of (Ni, Fe)-rich, Ti-rich-based phase and some pores. Here, the observed NiTi phase favored the shape memory behaviors.
- ii. Densification and hardness enhance significantly with an increase in sintering temperature due to a decrease in porosity. The 4 at. pct Fe sample sintered at 1200 °C shows higher density, lower porosity, and a higher hardness value compared to other compositions and other sintered samples. Densification favors the shape memory behavior of the sample.
- iii. The higher compressive and yield strength values of the sample sintered at 1100 °C were 62.65 MPa and 56.11 MPa, respectively, for the 8 at. pct Fe sample, and these values increased to 132.57 MPa and 116.86 MPa, respectively, for the 4 at. pct Fe sample sintered at 1150 °C.
- iv. The friction coefficient values of the alloy decreased significantly from 1100 °C to 1200 °C. SEM analyses of the worn surface of samples show an abrasive wear mechanism. NiTi phases help to absorb the stress during abrasion and decrease the coefficient of friction.
- v. The 6 at. pct Fe sample sintered at 1200 °C shows a higher shape memory effect of 3.37 pct than other compositions and other sintered samples. By increasing the sintering temperature, the minimum recovery percentage present is in 2 at. pct Fe, and it gradually increases up to 6 at. pct Fe and then gradually decreases in 8 at. pct Fe and 10 at. pct Fe. According to the analysis, the best sintering temperature among the three temperatures for a 4 h holding time is 1200 °C to get better shape memory behavior. However, based on the sample shape for 4 h holding time, 1150 °C is the best sintering temperature.

ACKNOWLEDGMENTS

This is a part of academic research work and is under the support of the Department of Metallurgical and Materials Engineering, National Institute of Technology, Rourkela, India.

AUTHOR CONTRIBUTIONS

All authors are agreed to the publication of the above manuscript. The contribution of all the authors is given below: JP: writing-original draft preparation, data accumulation, analysis, SCM: supervision, execution, and AB: conceptualist, analysis, supervision, review, modification.

CONFLICT OF INTEREST

This manuscript is original, unpublished, and not submitted to another journal. There is no conflict of interest in this journal. There is no source of funding associated with this paper. All authors agreed to submit this research paper.

REFERENCES

1. G.P. Cheng, Z.L. Xie, and Y. Liu: *J. Alloys Compd.*, 2006, vol. 415, pp. 182–87. <https://doi.org/10.1016/j.jallcom.2005.08.014>.
2. G.S. Firstov, J. Van Humbeeck, and Y.N. Koval: *J. Intell. Mater. Syst. Struct.*, 2006, vol. 17, pp. 1041–047. <https://doi.org/10.1177/1045389X060063922>.
3. J. Parida and S.C. Mishra: *NiTi-Based Ternary Alloys*, Elsevier, New York, 2022, pp. 191–213.
4. K. Otsuka and X. Ren: *Prog. Mater. Sci.*, 2005, vol. 50, pp. 511–678. <https://doi.org/10.1016/j.pmatsci.2004.10.001>.
5. T. H. M. Matsumoto: 1st JIM Int. In Symp. on Martensite, Kobe, Japan, 1976, vol. 199.
6. M.-S. Choi, T. Fukuda, and T. Kakeshita: *Scr. Mater.*, 2005, vol. 53, pp. 869–73. <https://doi.org/10.1016/j.scriptamat.2005.05.040>.
7. Shape Memory Alloy Research Team (Smart), <http://smart.tamu.edu>, no. <http://smart.tamu.edu>, p., 2001.
8. H. Nakajima and M. Koiwa: *ISIJ Int.*, 1991, vol. 31, pp. 757–66. <https://doi.org/10.2355/isijinternational.31.757>.
9. T. Hara, T. Ohba, E. Okunishi, and K. Otsuka: *Mater. Trans. JIM*, 1997, vol. 38, pp. 11–7. <https://doi.org/10.2320/matertrans1989.38.11>.
10. I. Yoshida, D. Monma, and T. Ono: *J. Alloys Compd.*, 2008, vol. 448, pp. 349–54. <https://doi.org/10.1016/j.jallcom.2007.04.217>.
11. S. Xue, W. Wang, D. Wu, Q. Zhai, and H. Zheng: *Mater. Lett.*, 2012, vol. 72, pp. 119–21. <https://doi.org/10.1016/j.matlet.2011.12.095>.
12. J.L. Lemanski: *AIP Conf. Proc.*, 2006, vol. 824, pp. 3–10. <https://doi.org/10.1063/1.2192327>.
13. T. Ogawa, K. Yokoyama, K. Asaoka, and J. Sakai: *Mater. Sci. Eng. A*, 2005, vol. 393, pp. 239–46. <https://doi.org/10.1016/j.msea.2004.10.020>.
14. S. Aksöz: *Arab. J. Sci. Eng.*, 2017, vol. 42, pp. 2573–581. <https://doi.org/10.1007/s13369-017-2567-2>.
15. S. Aksöz and B. Bostan: *Springer Proc. Phys.*, 2014, vol. 154, pp. 129–141. https://doi.org/10.1007/978-3-319-04639-6_18.
16. L. Krone, E. Schüller, M. Bram, O. Hamed, H.-P. Buchkremer, and D Stöver.: *Mater. Sci. Eng. A*, 2004, vol. 378, pp. 185–190. <https://doi.org/10.1016/j.msea.2003.10.345>.
17. C. Shearwood, Y. Q. Fu, L. Yu, and K. A Khor: *Scr. Mater.*, 2005, vol. 52, pp. 455–460. <https://doi.org/10.1016/j.scriptamat.2004.11.010>.

18. S.L. Zhu, X.J. Yang, F. Hu, S.H. Deng, and Z.D. Cui: *Mater. Lett.*, 2004, vol. 58, pp. 2369–373. <https://doi.org/10.1016/j.matlet.2004.02.017>.
19. B. Liu, Z. Liu, X. Liu, W. Wang, and L. Wang: *J. Alloys Compd.*, 2013, vol. 578, pp. 373–79. <https://doi.org/10.1016/j.jallcom.2013.05.164>.
20. A.A. Atyiah, A.-R.K.A. Ali, and N.M. Dawood: *Arab. J. Sci. Eng.*, 2015, vol. 40, pp. 901–13. <https://doi.org/10.1007/s13369-014-1538-0>.
21. H. Jiang, C. Ke, S. Cao, X. Ma, and X. Zhang: *Trans. Nonferrous Met. Soc. China*, 2013, vol. 23, pp. 2029–036. [https://doi.org/10.1016/S1003-6326\(13\)62692-8](https://doi.org/10.1016/S1003-6326(13)62692-8).
22. B.-Y. Li, L.-J. Rong, and Y.-Y. Li: *Intermetallics*, 2000, vol. 8, pp. 643–46. [https://doi.org/10.1016/S0966-9795\(99\)00140-5](https://doi.org/10.1016/S0966-9795(99)00140-5).
23. S. Aksöz, A.T. Özdemir, and B. Bostan: *J. Fac. Eng. Archit. Gazi Univ.*, 2012, vol. 27, pp. 109–15.
24. S. Aksöz and B. Bostan: *J. Polytech.*, 2018, <https://doi.org/10.2339/politeknik.389617>.
25. B.B.S. Aksöz, Ü. Demir, H. Ada, and H. Gökmeşe: *GU J. Sci. Part C*, 2017, vol. 5, pp. 99–106.
26. T. Mousavi, F. Karimzadeh, and M.H. Abbasi: *Mater. Sci. Eng. A*, 2008, vol. 487, pp. 46–51. <https://doi.org/10.1016/j.msea.2007.09.051>.
27. M. Karolus and J. Panek: *J. Alloys Compd.*, 2016, vol. 658, pp. 709–15. <https://doi.org/10.1016/j.jallcom.2015.10.286>.
28. R. Liu and D.Y. Li: *Mater. Sci. Technol.*, 2000, vol. 16, pp. 328–32. <https://doi.org/10.1179/026708300101507730>.
29. D.Y. Li and X. Ma: *J. Mater. Sci. Technol.*, 2001, vol. 17, pp. 45–6.
30. R. Neupane and Z. Farhat: *Wear*, 2013, vol. 301, pp. 682–87. <https://doi.org/10.1016/j.wear.2012.11.017>.
31. X.W. Huang, G.N. Dong, and Z.R. Zhou: *J. Mater. Eng*, 2004, vol. 6, pp. 41–3.
32. G. Tang, D. Zhang, J. Zhang, P. Lin, and G. Dong: *Appl. Surf. Sci.*, 2014, vol. 321, pp. 371–77. <https://doi.org/10.1016/j.apsusc.2014.09.151>.
33. L. Yan and Y. Liu: *J. Mater. Res.*, 2015, vol. 30, pp. 186–96. <https://doi.org/10.1557/jmr.2014.381>.
34. H.W. Jin: *Acta Metall. Sin.*, 1988, vol. 1, pp. 76–81.
35. Y.N. Liang, S.Z. Li, Y.B. Jin, W. Jin, and S. Li: *Wear*, 1996, vol. 198, pp. 236–41. [https://doi.org/10.1016/0043-1648\(96\)06989-X](https://doi.org/10.1016/0043-1648(96)06989-X).
36. D.Y. Li: *Scr. Mater.*, 1996, vol. 34, p. 195.
37. W. Ni, Y.-T. Cheng, M.J. Lukitsch, A.M. Weiner, L.C. Lev, and D.S. Grummon: *Appl. Phys. Lett.*, 2004, vol. 85, pp. 4028–030. <https://doi.org/10.1063/1.1811377>.
38. E. Rabinowicz and R.I. Tanner: *J. Appl. Mech.*, 1996, vol. 33, pp. 479–79. <https://doi.org/10.1115/1.3625110>.
39. J. Singh and A.T. Alpas: *Wear*, 1995, vol. 181–183, pp. 302–11. [https://doi.org/10.1016/0043-1648\(95\)90037-3](https://doi.org/10.1016/0043-1648(95)90037-3).
40. L. Yan, Y. Liu, and E. Liu: *Tribol. Int.*, 2013, vol. 66, pp. 219–24. <https://doi.org/10.1016/j.triboint.2013.05.012>.
41. J. Parida, S.C. Mishra, and A. Behera: *Met. Mater. Int.*, 2022, <https://doi.org/10.1007/s12540-022-01277-7>.
42. M. Farvizi, T. Ebadzadeh, M.R. Vaezi, E.Y. Yoon, Y.-J. Kim, J.Y. Kang, H.S. Kim, and A. Simchi: *Wear*, 2015, vol. 334–335, pp. 35–43. <https://doi.org/10.1016/j.wear.2015.04.011>.
43. F. Alijani, R. Amini, M. Ghaffari, M. Alizadeh, and A.K. Okyay: *Mater. Des.*, 2014, vol. 55, pp. 373–80. <https://doi.org/10.1016/j.matdes.2013.09.009>.
44. J.L. Xu, X.F. Jin, J.M. Luo, and Z.C. Zhong: *Mater. Lett.*, 2014, vol. 124, pp. 110–12. <https://doi.org/10.1016/j.matlet.2014.03.088>.
45. F. Zhang, L. Zheng, Y. Wang, and H. Zhang: *Intermetallics*, 2019, vol. 112, p. 106548. <https://doi.org/10.1016/j.intermet.2019.106548>.
46. T.-S. Huang, S.-F. Ou, C.-H. Kuo, and C.-H. Yang: *Metals (Basel)*, 2020, <https://doi.org/10.3390/met10040527>.
47. J. De Keyzer: *Thermodynamic Modeling of the Fe-Ni-Ti System: A Multiple Sublattice Approach*. University of Leuven, 2008.
48. M. Matsumoto, and T. Honma: 1st JIM Int, In *Symp. on Martensite, Kobe, Japan*, 1976, pp. 199.
49. N. Zhang, K.P. Babayan, and J.H. Lindenhovius: *Mater. Sci. Eng. A*, 1992, vol. 150, pp. 263–70.
50. Archimedes' Principle, in: n.d, pp. 37–38.
51. <https://www.labdepotinc.com/articles/archimedes-principles.html>, 2019.
52. <https://www.andersonmaterials.com/density-and-porosity-measurements-of-solid-materials.html>, 2020.
53. J.Y. Choi and S. Nemat-Nasser: *Mater. Sci. Eng. A*, 2006, vol. 432, pp. 100–07. <https://doi.org/10.1016/j.msea.2006.05.155>.
54. W. Bolton: *Engineering Materials Technology*, 2nd eds. Butterworth Heinemann Oxford, 2013.
55. ASTM Designation E 384-99, ASTM, *Philadelphia PA*, 1999.
56. G.E. Dieter: *Mechanical metallurgy. Mech Metall.*, 2011, <https://doi.org/10.5962/bhl.title.35895>.
57. I. Manika and J. Maniks: *Acta Mater.*, 2006, vol. 54, pp. 2049–056. <https://doi.org/10.1016/j.actamat.2005.12.031>.
58. Y. G. G.M. Pharr and E.G. Herbert: *Annu. Rev. Mater. Res*, 2010, p. 271.
59. N. Zhou, C. Shen, M.F.-X. Wagner, G. Eggeler, M.J. Mills, and Y. Wang: *Acta Mater.*, 2010, vol. 58(20), pp. 6685–694. <https://doi.org/10.1016/j.actamat.2010.08.033>.
60. L. Zhang, Y.Q. Zhang, Y.H. Jiang, and R. Zhou: *J. Alloys Compd.*, 2015, vol. 644, pp. 513–22. <https://doi.org/10.1016/j.jallcom.2015.05.063>.
61. S.L. Zhu, X.J. Yang, D.H. Fu, L.Y. Zhang, C. Li, and Z.D. Cui: *Mater. Sci. Eng. A*, 2005, vol. 408, pp. 264–68. <https://doi.org/10.1016/j.msea.2005.08.012>.
62. S. Waqar, A. Wadood, A. Mateen, and M.A.U. Rehman: *Int. J. Adv. Manuf. Technol.*, 2020, vol. 108, pp. 625–34. <https://doi.org/10.1007/s00170-020-05380-0>.
63. R. Shashanka, D. Chaira, and D. Chakravarty: *J. Mater. Sci. Eng. B*, 2016. <https://doi.org/10.17265/2161-6221/2016.5-6.001>.
64. E. Rabinowicz, *Friction and Wear of Materials*, John Wiley & Sons, Inc., New York, 1995, pp. 65–123.
65. Y. Wen, Y.-F. Wang, H. Ran, W. Wei, J.-M. Zhang, and C.-X. Huang: *Acta Metall. Sin.*, 2022, vol. 35(2), pp. 317–25.
66. M. Whitney, S.F. Corbin, and R.B. Gorbet: *Acta Mater.*, 2008, pp.559–570.

Publisher's Note Springer Nature remains neutral with regard to jurisdictional claims in published maps and institutional affiliations.

Springer Nature or its licensor (e.g. a society or other partner) holds exclusive rights to this article under a publishing agreement with the author(s) or other rightsholder(s); author self-archiving of the accepted manuscript version of this article is solely governed by the terms of such publishing agreement and applicable law.